EDGE ARTICLE

Check for updates

Hierarchical polar–nonpolar phase architecture enabling excellent lead-free capacitive energy storage

Qingqing Wu,[a] Huajie Luo,*[b] Yuhang Hu,[a] Yuhui Huang,[c] Xiangwei Guo,*[c] Hubo Zhu,[a] Haishan Xu,[a] Shenglin Jiang,[d] Tianyu Li [ID] *[be] and Bing Xie [ID] *[a]

Dielectric capacitors are highly attractive for advanced power electronics owing to their ultrafast charge–discharge rate, high power density, and excellent reliability. Yet their application is hindered by the persistent trade-off between high recoverable energy density (W_{rec}) and high efficiency (η) owing to the inherent coupling in single-phase dielectrics, where stronger polarization generally comes at the expense of higher hysteresis and limited breakdown strength. Here, we present a polar–nonpolar hierarchical phase architecture design in $BaTiO_3$–$BiMg_{0.5}Ti_{0.5}O_3$-based ceramics to overcome this limitation by modulating thermodynamic spinodal decomposition. The polar Ba-rich phase provides large maximum polarization, while the non-polar Cd-rich precipitation with a large bandgap acts as a high-resistivity barrier that isolates polar regions and enhances the breakdown field. Atomic-scale electron microscopy analysis reveals that the nanoscale polar regions ($\sim$1–3 nm) with locally disordered configurations emerge in the ceramic, which lowers the energy barrier for domain switching and enables near-zero hysteresis losses. As a result, the optimized hierarchical composition achieves an ultrahigh efficiency of 92.8%, a high recoverable energy density of 9.7 J cm^{-3}, an outstanding high figure of merit W_F of 135 at 460 kV cm^{-1}, along with excellent stability against temperature, frequency, and cycling, and fast discharge with a power density up to 185 MW L^{-1}. This work demonstrates a robust design paradigm based on complementary dual-phase coexistence, offering fundamental insights and a practical pathway toward high-performance, lead-free dielectric capacitors.

1. Introduction

Dielectric capacitors are indispensable for modern electronic and electrical systems due to their ultrafast charge–discharge speed, high power density, and long-term reliability.[1–4] Their energy storage performance is primarily determined by the recoverable energy density (W_{rec}) and efficiency (η), which can be defined as follows:[5–8]

$$W_{total} = \int_0^{P_{max}} E dP, \quad W_{rec} = \int_{P_r}^{P_{max}} E dP, \quad \eta = \frac{W_{rec}}{W_{total}},$$

where W_{total}, P_{max}, P_r and E represent the total energy density, maximum polarization, remnant polarization and applied electric field, respectively. In this case, achieving excellent overall energy

storage performance requires dielectrics with a high breakdown strength (E_b) and a large polarization difference ($\Delta P = P_{max} - P_r$). However, the widely developed single-phase ferroelectrics face an intrinsic conflict: enhancing polarization tends to increase remanent polarization and hysteresis, while improving breakdown strength typically requires suppressing polarization.[9–12] This trade-off has become the major bottleneck restricting the practical deployment of high-energy-density, high-efficiency capacitors.

In recent years, significant efforts have been devoted to overcoming this limitation in single-phase relaxor ferroelectrics through structural and compositional engineering. Typical strategies include chemical substitution to tune ionic size and valence, domain engineering to manipulate switching dynamics, high-entropy design to stabilize multiple configurations, and the construction of superparaelectric states to suppress long-range order.[13–19] These approaches have successfully improved energy storage density and efficiency in various $BaTiO_3$-,[20–24] $(Bi_{0.5}Na_{0.5})TiO_3$-,[25–27] $BiFeO_3$-,[28–31] and $NaNbO_3$-[32–35] based systems. Nevertheless, most of these strategies involve increasingly complex multi-component chemistries, which not only raise processing costs but also compromise phase stability and reproducibility, hindering

[a]*School of Power and Energy, Jiangxi Key Laboratory of Green General Aviation Power, Nanchang Hangkong University, Nanchang 330063, China. E-mail: xieb@nchu.edu.cn*

[b]*School of Materials Science and Engineering, University of Science and Technology Beijing, Beijing 100083, China. E-mail: hjluo@ustb.edu.cn; tianyuli@ustb.edu.cn*

[c]*State Key Laboratory of Silicon and Advanced Semiconductor Materials, School of Materials Science and Engineering, Zhejiang University, Hangzhou, Zhejiang 310058, China. E-mail: l240441@zju.edu.cn*

[d]*School of Integrated Circuits, Huazhong University of Science and Technology, Wuhan 430074, China*

[e]*Department of Physics, City University of Hong Kong, Hong Kong SAR, China*

large-scale practical application. Against this backdrop, the introduction of a secondary phase into perovskite ceramics has emerged as a promising alternative design route. By combining phases with distinct functionalities, dual-phase systems can simultaneously regulate polarization and breakdown behavior, leveraging the combination of advantages from different dielectric phases, offering a new pathway beyond the limitations in single-phase ferroelectrics and dielectrics.[36–39] Traditional two-phase composites or core–shell structures employ components that do not react with each other and do not form solid solutions, (*e.g.*, perovskite ferroelectrics with SiO_2 or MgO),[40,41] leading to limited phase selection, structural discontinuities, and complex interfacial effects, while requiring delicate control of microstructure (core size, shell thickness) and coating/sintering process. By contrast, the polar–nonpolar hierarchical phase architecture forms *in situ via* thermodynamically driven phase separation, producing stable microstructures that enable complementary dielectric response rather than simple superposition.

Here, we propose a hierarchical polar–nonpolar phase architecture in $BaTiO_3$–$Bi(Mg_{0.5}Ti_{0.5})O_3$ (BT–BMT)-based ceramics, in which polar and non-polar phases, formed by spinodal decomposition, play complementary roles to promote energy storage. The polar Ba-rich phase provides large reversible polarization, while the non-polar Cd-rich phase acts as a high-resistivity barrier that enlarges the bandgap, suppresses

leakage, and reduces hysteresis (H) (Fig. 1a). To achieve this configuration, $CdZrO_3$ (CZ) was incorporated into the 0.5BT–0.5BMT matrix. The smaller ionic radius of Cd^{2+} (1.31 Å) relative to Bi^{3+} (1.34 Å) and Ba^{2+} (1.61 Å), combined with the chemical potential difference and limited mutual solubility between $CdZrO_3$ and the matrix, drives thermodynamically favored phase separation at the grain level. This synergistic dual-phase structure overcomes the intrinsic trade-off between energy density and efficiency, enabling the optimized 0.5BT–0.3BMT–0.2CZ composition to achieve an ultrahigh η of 92.8% at 460 kV cm^{-1}, a high W_{rec} of 9.7 J cm^{-3}, a corresponding high figure of merit W_F of 135, an excellent temperature/frequency/cycling stability, and rapid discharge with a power density of 185 MW L^{-1}. These results establish a robust design paradigm based on *in situ* dual-phase coexistence, providing mechanistic insight and a practical route toward high-performance, lead-free dielectric capacitors.

2. Results and discussion

To verify the feasibility of the proposed dual perovskite-phase design, ceramics were synthesized according to the designed molar ratios using conventional solid-state reaction. X-ray diffraction (XRD) analysis (Fig. 1b and S1) revealed a transformation from a single tetragonal phase to two sets of perovskite diffraction patterns, with no detectable impurity peaks.
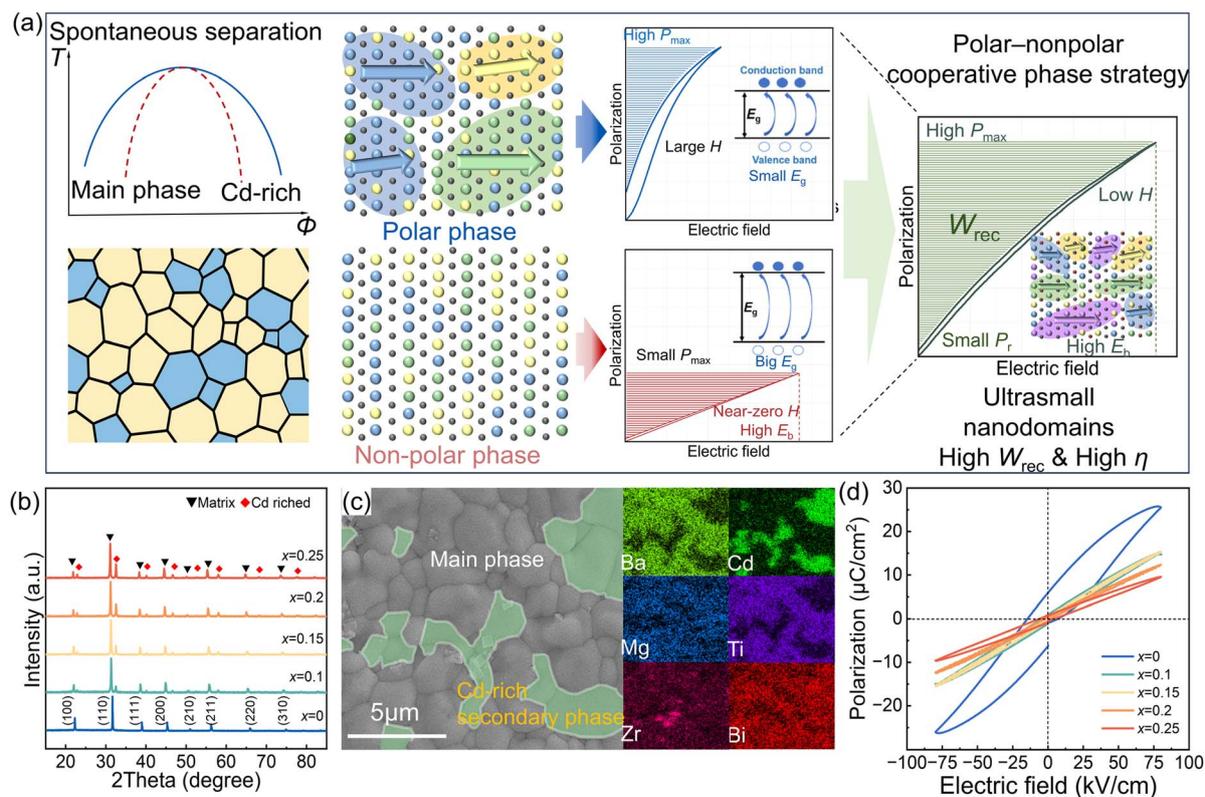

Fig. 1 (a) Design a polar−nonpolar hierarchical phase architecture in a relaxor oxide *via* modulating spinodal decomposition to achieve dual-high energy-storage capability. (b) XRD patterns of 0.5BT−(0.5 − x)BMT−xCZ ceramics. (c) A typical SEM morphology and element mappings of x = 0.2 ceramics. (d) Polarization−electric field (P−E) hysteresis loops of 0.5BT−(0.5 − x)BMT−xCZ ceramics.

The phase with the larger lattice parameter corresponds to the BT–BMT matrix phase, whereas the smaller-lattice phase is identified as the Cd-rich secondary phase, confirming successful formation of a dual-phase structure. Compared with physical composite based on insoluble and non-reactive constituents, as well as chemical substitution that introduce random fields to enhance relaxation,[40,42,43] the present approach enables the spontaneous formation of two phases with distinct dielectric responses from a single perovskite parent lattice, driven by intrinsic differences in ionic radius, diffusion kinetics, and chemical potential among constituent ions. Scanning electron microscopy (SEM) coupled with elemental mapping further revealed a dense microstructure without obvious pores or impurities (Fig. 1c, S2 and S3). Two distinct grain types were observed: the Cd-rich grains, outlined in white, are randomly embedded and interconnected within the matrix phase, forming a 3–3-type composite structure that directly influences electrical breakdown performance (Fig. 1c). Elemental maps and energy dispersive spectroscopy (EDS) analysis show clear compositional segregation: Ba is concentrated in the primary perovskite phase, Cd in the secondary phase, while Ti, Mg, Zr, and Bi are homogeneously distributed

(Fig. 1c). This segregation drives grain-level-separated dual perovskite-phase formation, consistent with XRD results. SEM and EDS analyses for the $x = 0.2$ ceramic subjected to high-temperature aging for 3 hours further show that the Cd distribution remained consistent with the as-prepared state, with no evidence of additional precipitation or phase separation, confirming the robustness of the designed polar–nonpolar two-phase architecture (Fig. S4). P–E loops measurements (Fig. 1d) show that the 0.5BT–0.5BMT material exhibits typical ferroelectric behavior with relaxor features, resulting from ionic size differences at the A and B sites. Upon $CdZrO_3$ incorporation, the P–E loops become slimmer and more linear, indicating a pronounced reduction in hysteresis and nonlinearity. At $x = 0.2$ under 80 kV cm^{-1}, the maximum polarization reaches 12.4 μC cm^{-2}, while the hysteresis is reduced to below 5%. These changes simultaneously demonstrate the non-polar nature of the grain-level-separated Cd-rich secondary phase, which could suppress energy loss, stabilize polarization, and mitigate the intrinsic nonlinear response to electric field, thereby suggesting an enhanced energy storage potential, especially for the $x = 0.2$ system.
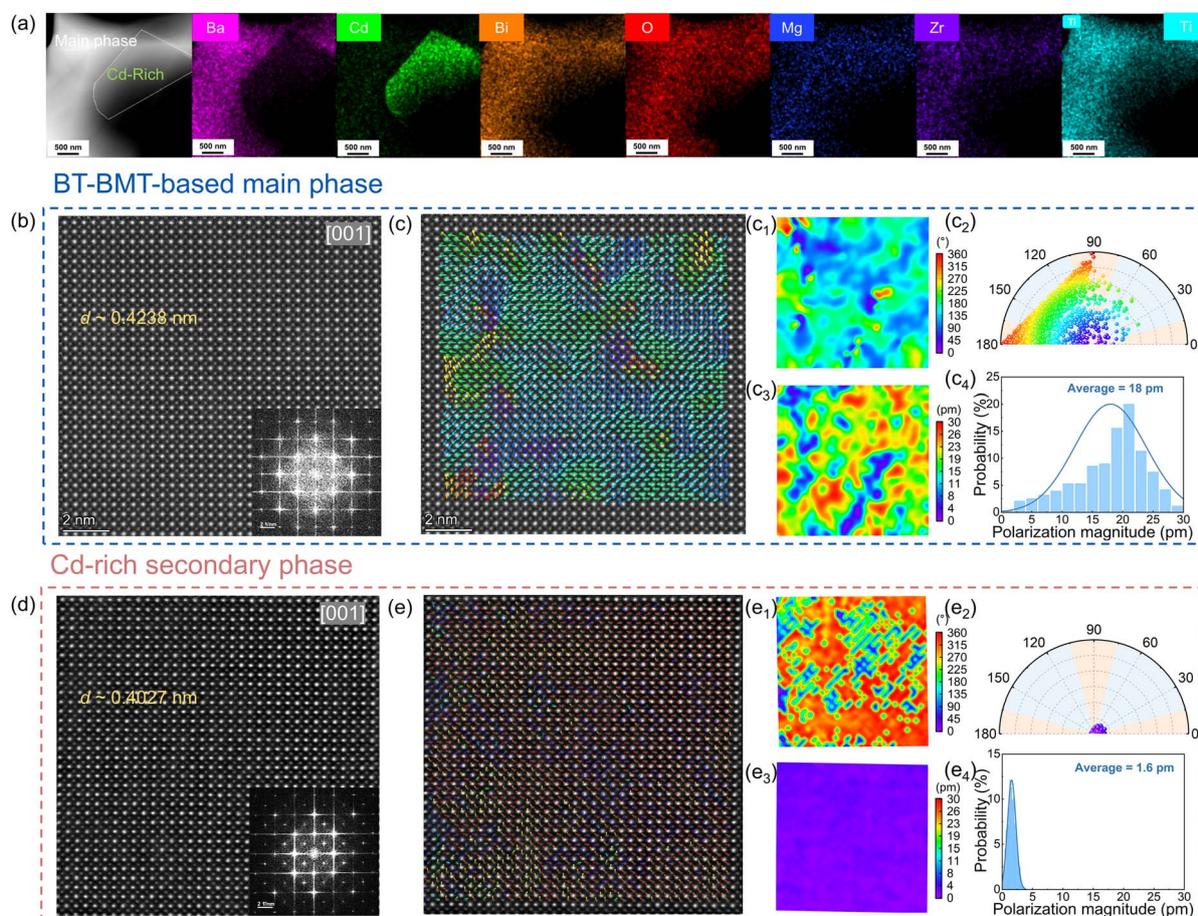

Fig. 2 (a) STEM-EDS mapping images of $x = 0.2$ ceramic; (b and d) HAADF-STEM images of main phase and Cd-rich phase in $x = 0.2$ ceramic along [001]$_c$ zone axis. (c) and (e) is atomic displacement vector mappings of main phase and Cd-rich phase in $x = 0.2$ ceramic. The insets in (b) and (d) represent the FFT diffraction patterns; [001]$_{pc}$ polarity angle distribution diagram and statistical diagram: (c$_1$ and c$_2$) main phase, (e$_1$ and e$_2$) Cd-rich phase; [001]$_{pc}$ polarity amplitude distribution chart and statistical chart: (c$_3$ and c$_4$) main phase, (e$_3$ and e$_4$) Cd-rich phase.

To clarify the polarization configurations and local structural features of the coexisting phases, we carried out a detailed atomic-scale scanning transmission electron microscopy (STEM) investigation on the $x = 0.2$ dual-phase ceramic. The STEM-EDS mapping images further confirmed the presence of the BT–BMT matrix phase alongside the Cd-rich secondary phase (Fig. 2a). Fig. 2b and d shows high-angle annular dark-field STEM (HAADF-STEM) along the $[001]_{pc}$ zone axis. No superlattice reflections are observed in the corresponding fast Fourier transformation (FFT) patterns of the BT–BMT matrix and Cd-rich phases (insets in Fig. 2b and d). This indicates the absence of long-range oxygen-octahedral tilting and concurrent ferroelectric ordering in both phases (Fig. 2b and d), consistent with the characteristic of relaxor ferroelectrics. The measured crystal-plane spaces further confirm the pseudo-cubic nature of both phases. The Cd-rich nonpolar phase exhibits a noticeably smaller lattice parameter ($a = 4.027$ Å) (Fig. 2d), whereas the polar matrix phase shows a larger value ($a = 4.238$ Å) (Fig. 2b), highlighting the lattice mismatch between the two coexisting phases and agreeing with the XRD characterizations. Quantitative c/a ratio mapping further reveals values very close to unity

in Cd-rich phase ($c/a \sim 1$, see Fig. S5, confirming that it adopts pseudo-cubic symmetry rather than developing a tetragonal distortion. This structural homogeneity provides a stable framework in which local polar heterogeneity can be accommodated.[44]

Quantitative polarity-vector mapping (Fig. 2c and e) provides further insights into the distribution of polarization and its differences between the two phases. The arrows denote the orientations of local polarization vectors, while their lengths correspond to the magnitudes. Within the polar main phase, island-like clusters with sizes of 1–3 nm are observed, which correspond to ultrafine polar nanoregions (PNRs) (Fig. 2c). These PNRs are spatially confined yet polymorphic in orientation, resulting in a broad distribution of polarization angles (Fig. 2c$_1$ and c$_2$). Such polymorphic PNRs are highly dynamic, which weakens the anisotropy of polarization orientation, lowers the energy barriers for domain-wall movement, and thereby facilitates smoother and more reversible domain re-orientation under applied electric fields. In contrast, the Cd-rich nonpolar phase remains free of long-range polarization (Fig. 2e and e$_1$–e$_{41}$-e$_4$), effectively acting as a structural matrix that
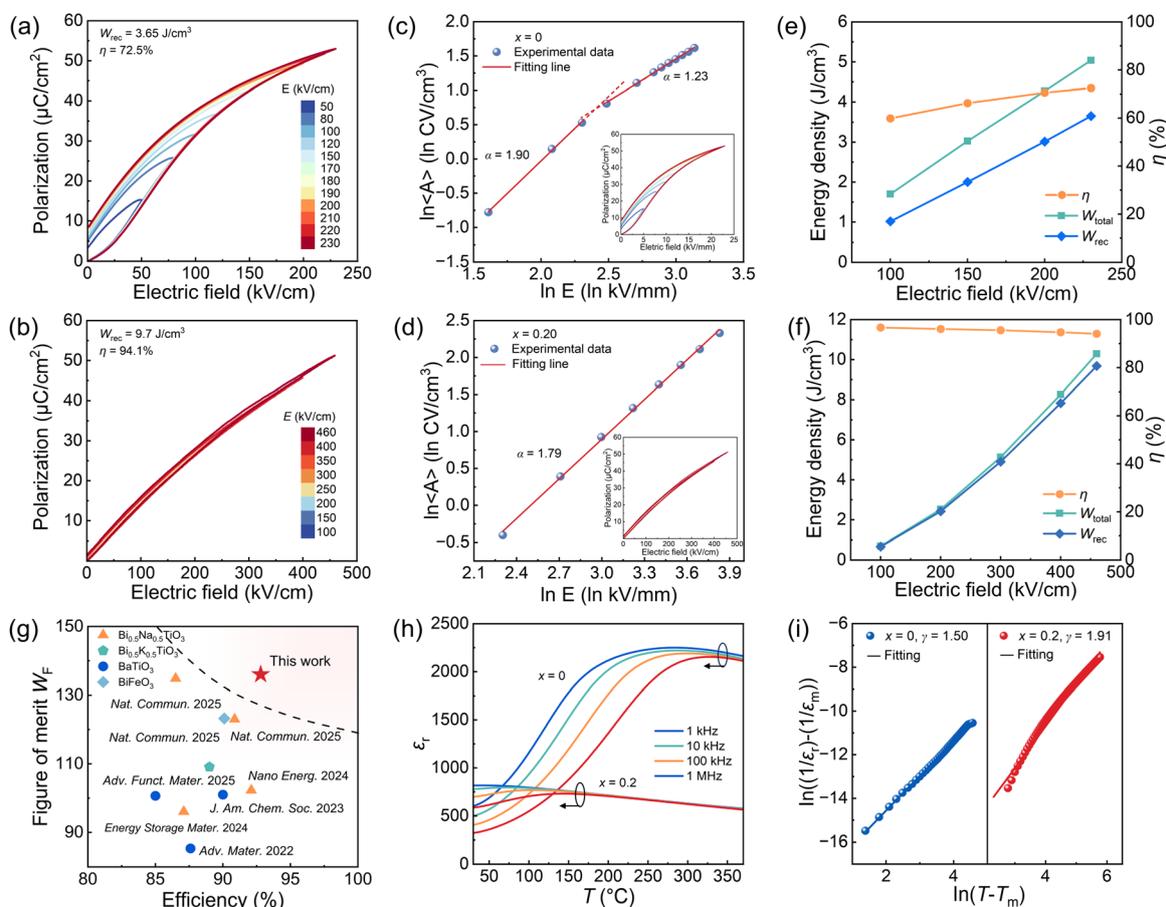

Fig. 3 Comparative analysis of dielectric energy-storage performance between $x = 0$ and 0.2 ceramics. (a and b) Unipolar P–E loops of $x = 0$ and 0.2 ceramics under breakdown field. (c and d) The curves of ln ⟨A⟩ as a function of ln E for the $x = 0$ and 0.2 ceramics, derived from their P–E loops under different electric fields at room temperature. (e and f) The variations of W_{total}, W_{rec} and η of $x = 0$ and 0.2 ceramics with electric field. (g) Comparison between the figure of merit W_F and η values for the representative lead-free bulk ceramics. (h) Temperature dependence of the dielectric constant of $x = 0$ and 0.2 ceramics. (i) Relaxor degree γ of $x = 0$ and 0.2 ceramics determined by Curie–Weiss fitting in (h).

accommodates polar clusters without imposing rigid constraints. This coexistence of nonpolar and polar regions gives rise to markedly different polarization amplitudes (Fig. $2c_3$, c_4, e_3 and e_{43}-c). In the polar regions, the average polarization amplitude reaches 1.6 pm, whereas the stronger matrix-like regions show a significantly larger value of 18.0 pm very close to the background signal. The combination of strongly and weakly polarized regions introduces both stability and flexibility into the system. According to Landau theory,[30,45,46] nanoscale domains with weak inter-domain interactions yet strong polarization strength can readily relax back to their initial configurations once the external field is removed. This spontaneous relaxor minimizes remanent polarization, suppresses hysteresis, and simultaneously preserves the capacity for high maximum polarization. Collectively, the results reveal that at $x = 0.2$ the ceramic develops a distinctive dual-phase configuration, wherein a Cd-rich nonpolar phase is characterized by reduced lattice dimensions and the absence of spontaneous polarization, and a polar pseudo-cubic matrix possesses highly active, polymorphic PNRs at the nanometer scale. Such a hierarchical microstructure effectively suppresses long-range ferroelectric ordering while enabling localized polar activity, thereby reducing hysteresis losses and enhancing energy-storage efficiency under high electric fields.

The energy-storage performance of different components was systematically investigated through comparative P–E loops measurements at their respective breakdown fields (Fig. 3a and b). With increasing $CdZrO_3$ content, the loop shape evolves markedly. For the $x = 0$ single phase, the loop is characterized by a large P_r and a narrow maximum applied field, indicative of limited energy-storage capability (Fig. 3a and e). By contrast, at $x = 0.2$ the P–E loop becomes slim, with P_r values approaching zero across the entire applied field range. Of equal importance is that the maximum electric field that can be applied to the $x = 0.2$ ceramic is significantly higher (460 kV cm^{-1}) than that of the pure $x = 0$ ceramic. This increase in withstanding field strength

demonstrates that the introduction of the Cd-rich nonpolar phase effectively enhances the dielectric breakdown resistance of the system. Building upon these observations, the $x = 0.2$ ceramic exhibits markedly improved energy-storage performance (Fig. 3b and f). It achieves a large P_{max} of 51.3 µC cm^{-2} while retaining an ultralow P_r of only 1.7 µC cm^{-2}, compared with $P_r = 7.36$ µC cm^{-2} for the pure main phase (Fig. 3a and b). To reveal the inherent differences in the dynamic polarization responses, we analyzed the P–E loops of different samples using the power-law relationship ($\langle A \rangle \propto E^a$).[47,48] $\langle A \rangle$ represents the energy dissipation within one cycle of polarization reversal, which is considered as a characteristic parameter of the dynamic behavior in FEs, while the exponent α is mainly controlled by the domain state and polarization switching mechanism. As shown in Fig. 3c, when $x = 0$, the ln E–ln $\langle A \rangle$ relationship clearly exhibits two stages: In the first stage, polarization rises rapidly owing to the domain switching, wherein the large hysteresis leads to a large α value. In the second stage, the linear extension happens, corresponding to a slow polarization growth and low hysteresis with small α value. These two stages thereby give rise to an evident non-linear P–E loop and low W_{rec}. By comparison, the ceramic with $x = 0.2$ only shows a single linear relationship throughout the entire measurement field range. Such behavior is owing to a continuous polarization evolution by merging these two processes, indicating a highly dynamic nanodomain for dual-high W_{rec} and η. To further determine the dynamic evolution of under an external electric field, phase-field simulations were conducted on $x = 0.2$ ceramic (Fig. S6 and S7). The initial PNR morphology in the phase-field model was constructed based on the STEM observations, reproducing the ultrafine polar nanoregions with 1–3 nm size distribution. Upon increasing the electric field, the polarization within individual PNRs progressively aligns with the field direction and undergoes continuous growth and coalescence, leading to a macroscopic polarization response characterized by low hysteresis and relaxor behavior in

Table 1 A comparison of W_F, W_{rec} and η between 0.5BT−0.3BMT−0.2CZ and other reported lead-free bulk ceramics[52,55,56,59,61–64]

Composition	W_F	W_{rec} (J cm^{-3})	η (%)	E_b (kV cm^{-1})	Temperature stability	Ref.
$0.92(Bi_{0.5}Na_{0.5})_{0.7}Sr_{0.3}TiO_3–0.08Ca(Mg_{1/3}Ta_{2/3})O_3$	68.1	8.37	87.7	530	$\Delta W_{rec} < 1.9\%$ $\Delta \eta < 10.35\%$	61
$(Sr_{0.24}Na_{0.1}Bi_{0.26}Ca_{0.2}\square_{0.2})TiO_3(\square: Sr$ vacancies$)$	75	6	92	440	$\Delta W_{rec} < 15\%$ $\Delta \eta < 15\%$	62
$0.82(0.5Bi_{0.5}K_{0.5}TiO_3–0.5Bi_{0.5}Na_{0.5}TiO_3)–0.18NaTaO_3$	75	15	80	740	$\Delta W_{rec} < 4.1\%$ $\Delta \eta < 3.10\%$	63
$0.65Na_{0.5}Bi_{0.5}TiO_3–0.35SrTiO_3$	95	7.6	92	620	$\Delta W_{rec} < 4\%$ $\Delta \eta < 8\%$	64
$0.75Bi_{0.5}Na_{0.5}TiO_3–0.25K_{0.5}Na_{0.5}NbO_3$	96.1	12.4	87.1	713	$\Delta W_{rec} < 0.08\%$ $\Delta \eta < 0.6\%$	56
$[Ba_{0.7}(Bi_{0.5}Na_{0.5})_{0.3}][Ti_{0.88}(Zn_{1/3}Nb_{2/3})_{0.12}]O_3$	100.7	15.1	85	900	$\Delta W_{rec} < 2.9\%$ $\Delta \eta < 2.9\%$	55
$0.8(Bi_{0.5}Na_{0.25}K_{0.25})TiO_3–0.2BaZrO_3$	109.1	12	89	560	$\Delta W_{rec} < 5.4\%$ $\Delta \eta < 5\%$	52
$(Bi_{1/3}K_{1/6}Na_{1/6}Ba_{1/6}Sr_{1/6})(Ti_{0.8}Zr_{0.2})O_3$	124.6	18.7	85	770	$\Delta W_{rec} < 5\%$ $\Delta \eta < 10\%$	59
$0.5BaTiO_3–0.3BiMg_{0.5}Ti_{0.5}O_3–0.2CdZrO_3$	135	9.7	92.8	460	$\Delta W_{rec} < 2\%$ $\Delta \eta < 2\%$	This work

the P–E loop. Therefore, the simulation result further supports our experimental observation, being consistent with the analysis based on the power-law scaling relationship (Fig. 3c and d).

The energy storage performance was analyzed and compared. For $x = 0.2$ ceramic, its favorable polarization behavior, together with the improved voltage endurance, results in an outstanding W_{rec} of 9.7 J cm^{-3} and an exceptionally high η of 94.1%, in stark contrast to the $x = 0$ ceramic with W_{rec} of 3.65 J cm^{-3} and η of 72.5% (Fig. 3e and f). The multiple P–E loop measurements were performed on different ceramics, where the results show a good consistency with average $W_{rec} = 9.7$ J cm^{-3} and $\eta = 92.8\%$ (Fig. S8). In dielectric energy storage materials, W_{rec} and η of the material are usually described separately. Therefore, we use the figure of merit W_F to comprehensively evaluate the ability of the dielectric capacitors to store and release electric energy, which is defined as: $W_F = W_{rec}/(1 - \eta)$, where W_F represents the energy that the material can store under the unit loss and $(1 - \eta)$ represents the energy loss rate.[6] The higher W_F, the more energy the dielectric materials can store under the same loss. The high W_{rec} and η lead to high figure of merit W_F of 135. By comparing the comprehensive performance of representative lead-free dielectric ceramics and dual-phase/composite ceramics, it is evident that the designed dual-phase ceramic exhibits high performance level among them (Fig. 3g and Table 1, S1).[20,49–56] Taken together, these results highlight the designed dual-phase ceramic as a promising candidate for high-performance dielectric energy-storage applications.

To understand the dielectric characteristics closely correlated to the polarization behavior and energy-storage performance, we then measured the temperature-dependent dielectric spectra of the 0.5BT–(0.5 − x)BMT–xCZ composites multiple times (Fig. 3h and S9). It can be noted that all samples exhibit pronounced frequency dispersion, with the peak dielectric constant (ε_m) decreasing and the corresponding maximum temperature (T_m) shifting to higher temperatures as the measurement frequency increases. Increasing the CdZrO$_3$ content leads to a diffuse ferroelectric–paraelectric phase transition and shifts T_m to lower temperatures relative to the pure BT–BMT ceramics. These are typical relaxor features that originate from not only the presence of highly dynamic polar nanoregions in the main phase but also the contribution from the nonpolar secondary phase. The relaxor behavior of the materials was further evaluated using the modified Curie–Weiss law, expressed as:[22,57,58] $\gamma = (T - T_m)/C$, where C is a Curie-like constant, T is the measurement temperature, and γ quantifies the degree of diffuseness (the values of γ range from 0 to 1 corresponds to classical ferroelectrics, 1 to 2 for relaxor ferroelectrics and 2 corresponds to ideal relaxor ferroelectrics). As shown in Fig. 3i, the $x = 0.2$ ceramic exhibits the highest γ value of 1.91, exceeding 1.50 for the $x = 0$ single phase. The larger γ reflects stronger relaxor behavior and reduced hysteresis. Stronger relaxor allows PNRs to reorient more rapidly under an external electric field, which plays a crucial role in reducing P_r while maintaining high P_{max}. As evidenced by the repetitive measurements, the dielectric properties of the ceramic are stable, which also supports this conclusion (Fig. S10). These dielectric measurements therefore provide direct evidence that the coexistence of polymorphic PNRs and the nonpolar Cd-rich phase underlies the exceptional energy-storage performance observed in the $x = 0.2$ ceramics.

Since high E_b and excellent insulating properties play a key role in supporting superior energy-storage performance, electrical breakdown tests were therefore conducted for each sample and statistically validated using the Weibull distribution method (Fig. 4a). Consistent with previous unipolar P–E
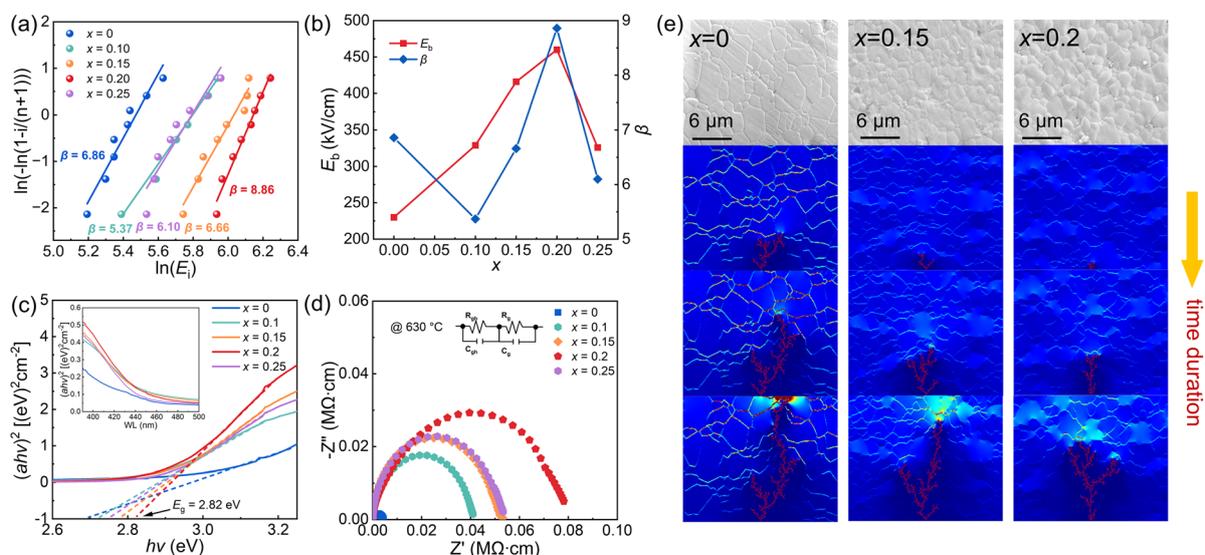

Fig. 4 (a) Weibull distribution of the breakdown electric field of the 0.5BT–(0.5 − x)BMT–xCZ ceramics. (b) E_b and β with regard to x. (c) Ultraviolet-visible (UV-vis) absorbance spectra of 0.5BT–(0.5 − x)BMT–xCZ ceramics. The inset displays an enlarged view of the $(\alpha h\nu)^2$–$h\nu$ curves. (d) Impedance spectra for $x = 0$, 0.1, 0.15, 0.2, and 0.25 ceramics measured at 630 °C. (e) Simulated real-time evolution of electric field distributions and the propagation of breakdown paths for $x = 0$, 0.15, and 0.2 ceramics.

loop measurements, the maximum E_b of 460 kV cm^{-1} is achieved for the $x = 0.2$ composition, and the Weibull modulus β of 8.86 further confirms high reliability and consistency for E_b (Fig. 4b).[59] To elucidate the factors influencing E_b, bandgap (E_g) and electrical resistance were evaluated, as they directly affect dielectric breakdown.[49,58] According to the empirical relationship for intrinsic breakdown strength ($E_b \propto e^{\sqrt{E_g}}$), a larger E_g hinders electron transitions from the valence band to the conduction band, contributing to higher E_b.[16,60] As shown in Fig. 4c, the $x = 0.2$ sample exhibits the largest E_g of 2.82 eV among all compositions. Impedance measurements and corresponding Nyquist plots recorded at 550–630 °C show that $x = 0.2$ has the largest Debye semicircle radius at 630 °C, indicating the highest electrical resistance (Fig. 4d and S11).

To further verify the experimental observations of breakdown behavior, finite-element simulations for the $0.5BT$–$(0.5 - x)BMT$–xCZ ceramics were conducted based on SEM images and dielectric temperature spectra. It is well known that strong electric fields tend to concentrate at grain boundaries due to their lower dielectric constant compared with the grains.[7,10] In the $x = 0$ composition, breakdown occurs rapidly, with electric

dendrites propagating throughout the entire sample. By contrast, in the $x = 0.15$ and $x = 0.2$ ceramics, where the grain-separated dual-phase design is realized, the growth rate of the electric tree slows down. When in $x = 0.2$, the electric tree extends only about two-thirds of the sample thickness (Fig. 4e), consistent with the higher breakdown field observed experimentally. This demonstrates that the deliberate incorporation of the highly insulating Cd-rich nonpolar phase into the dual-phase structure effectively separates grains, enhances local resistivity, and suppresses the propagation of breakdown pathways. Collectively, these results indicate that the improvement of E_b, the increase in E_g, and the elevated electrical resistance all originate from the high insulation provided by the Cd-rich phase, confirming the effectiveness of the proposed grain-separated dual-phase design in supporting superior energy-storage performance. The improved breakdown performance of the $x = 0.2$ sample correlates with its smaller grain size, lower ε_r, and the presence of two-phase contact grain boundaries, which are less prone to failure than the boundaries in the BT–BMT single phase. These simulation results confirm the experimental finding that introducing a dual-phase
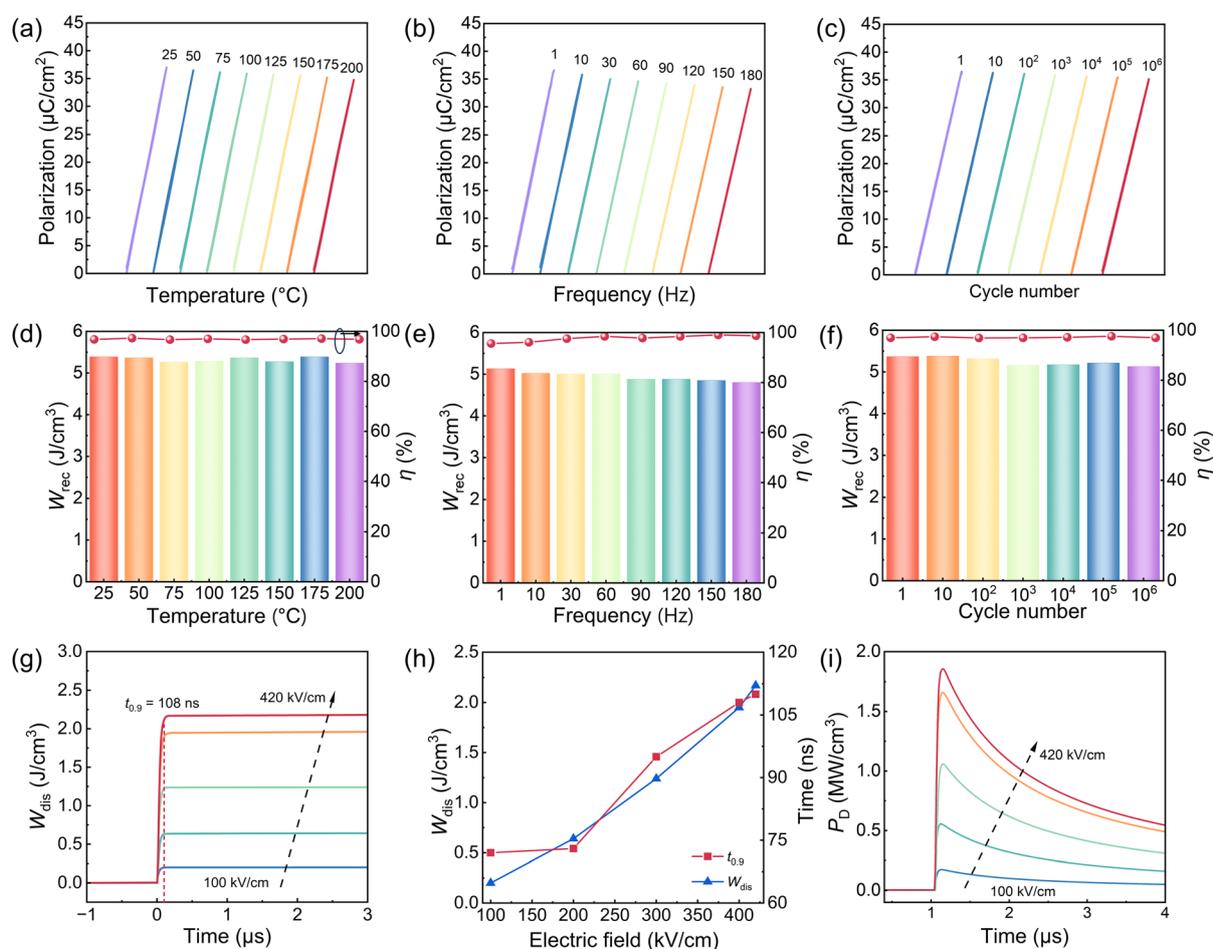

Fig. 5 Stability performance of the $x = 0.2$ ceramics. (a–c) Dependence of energy density and efficiency with respective to unipolar P–E loops of $x = 0.2$ ceramic as a function of temperature, frequency, and cycling number, respectively. (d–f) W_{rec} and η with respective to (a) and (d) temperature, (b) and (e) frequency, and (c) and (e) number of cycles extracted from (a–c). (g) Overdamped W_{dis} of $x = 0.2$ with a variation of the applied electric field. (h) W_{dis} and $t_{0.9}$ as a function of electric field. (i) Power density as a function of time.

coexistence system effectively enhances breakdown strength and supports the dual-phase design strategy.

Considering the practical requirements for dielectric capacitors to operate under diverse environments and conditions, we evaluated the temperature stability, frequency stability, and cycle stability of the $x = 0.2$ ceramics at an electric field of 300 kV cm^{-1}. The temperature stability was assessed from 25 °C to 200 °C (Fig. 5a and d), and the sample exhibits excellent performance, with the recoverable energy density and efficiency decreasing by less than 2% across the measured range. Frequency stability tests show minimal variation in recoverable energy density (4.96 ± 0.16 J cm^{-3}) and an efficiency change of only 2% over a broad frequency range of 1–180 Hz (Fig. 5b and e). Remarkably, the ceramics also demonstrate exceptional cycle stability, with negligible variation in recoverable energy density (5.13 ± 0.11 J cm^{-3}) and ultra-low efficiency change (0.2%) over 10 to 10^6 cycles, maintaining a recoverable energy density of 5.13 J cm^{-3} and efficiency of 97.1% even after 10^6 cycles (Fig. 5c and f). These results indicate that $x = 0.2$ ceramics possess excellent energy storage stability under various operational conditions, highlighting their suitability as high-performance dielectric capacitors.

To investigate the pulse charging and discharging capabilities and power densities of the $x = 0.2$ dual-phase ceramics, fast charging and discharging experiments were conducted. The slight decrease in efficiency at elevated temperatures is likely related to thermally induced conduction losses. Fig. 5g and h presents the room-temperature discharge energy density of $x = 0.2$ under different electric fields. As the applied electric field increases from 100 kV cm^{-1} to 420 kV cm^{-1}, the discharge energy density (W_{dis}) rises from 0.2 J cm^{-3} to 2.17 J cm^{-3}. The parameter $t_{0.9}$, representing the discharge time required to release 90% of the charged energy, is only 108 ns at 420 kV cm^{-1}, confirming rapid discharge capability. Correspondingly, the power density reaches a maximum of 185 MW L^{-1} at 420 kV cm^{-1} (Fig. 5i). Overall, these measurements strongly confirm that the $x = 0.2$ ceramics combine high energy-storage density, exceptionally high efficiency, and excellent stability with ultra-fast discharge capability, demonstrating considerable potential for practical dielectric capacitor applications.

3. Conclusion

In conclusion, taking 0.5BaTiO_3–$(0.5 - x)\text{Bi}(\text{Mg}_{0.5}\text{Ti}_{0.5})\text{O}_3$–$x\text{CdZrO}_3$ ceramics as an example, the hierarchical polar–nonpolar phase architecture effectively tailors both microstructural and local polarization heterogeneity to achieve superior energy-storage performance. The BaTiO_3–$\text{Bi}(\text{Mg}_{0.5}\text{Ti}_{0.5})\text{O}_3$ polar matrix within nanoscale polar regions and diverse polar orientations not only provides high reversible polarization but also reduces domain-switching barriers and suppresses hysteresis. As a comparison, the Cd-rich nonpolar phase contributes high insulation, enlarged bandgap, and enhanced breakdown strength, enabling the material to operate under high electric fields with extremely low energy loss. Therefore, this hierarchical dual-phase design offers a robust route to lead-free dielectric capacitors that combine high energy density,

ultralow losses, excellent stability, and rapid charge/discharge capability, providing both mechanistic insight and practical guidance for high-performance energy storage applications.

Conflicts of interest

There are no conflicts to declare.

Data availability

The data supporting this article have all been included in the main text and supplementary information (SI). Supplementary information: sample preparation, microstructural characterization, performance characterization, and related supplementary figures and tables. See DOI: https://doi.org/10.1039/d6sc00039h.

Acknowledgements

References

1 B. Xie, Z. Li, H. Luo, X. Shi, K. Wang, Z. Liu, K. Guo, H. Zhang, T. Li, Z. Cheng and S. Zhang, Constructing superrelaxor critical state towards giant energy storage in lead-free dielectric ceramics, *Nat. Commun.*, 2026, **17**, 1583.

2 Q. Chai, Z. Liu, Z. Deng, Z. Peng, X. Chao, J. Lu, H. Huang, S. Zhang and Z. Yang, Excellent energy storage properties in lead-free ferroelectric ceramics via heterogeneous structure design, *Nat. Commun.*, 2025, **16**, 1633.

3 B. Yang, Y. Liu, R.-J. Jiang, S. Lan, S.-Z. Liu, Z. Zhou, L. Dou, M. Zhang, H. Huang, L.-Q. Chen, Y.-L. Zhu, S. Zhang, X.-L. Ma, C.-W. Nan and Y.-H. Lin, Enhanced energy storage in antiferroelectrics via antipolar frustration, *Nature*, 2025, **637**, 1104–1110.

4 H. Liu, Z. Sun, J. Zhang, H. Luo, Y. Zhang, A. Sanson, M. Hinterstein, L. Liu, J. C. Neuefeind and J. Chen, Chemical Framework to Design Linear-like Relaxors toward Capacitive Energy Storage, *J. Am. Chem. Soc.*, 2024, **146**, 3498–3507.

5 Z. Wang, D. Li, W. Liu, L. He, D. Xu, J. Liu, J. Ren, X. Wang, Y. Liu, G. He, J. Bao, Z. Fang, G. Yan, X. Liang, T. Zhou, W. Zhao, W. Liu, D. Wang and D. Zhou, Ultra-high energy storage in lead-free NaNbO$_3$-based relaxor ceramics with directional slush-like polar structures design, *Nat. Commun.*, 2025, **16**, 2892.

6 L. Shu, X. Shi, X. Zhang, Z. Yang, W. Li, Y. Ma, Y.-X. Liu, L. Liu, Y.-Y.-S. Cheng, L. Wei, Q. Li, H. Huang, S. Zhang and J.-F. Li, Partitioning polar-slush strategy in relaxors

leads to large energy-storage capability, *Science*, 2024, **385**, 204–209.

7 Y. Hu, B. Xie, S. Wu, H. Zu, Z. Liu, K. Guo, P. Mao and H. Luo, Ultrahigh breakdown strength achieving exceptional recoverable energy storage density in NaNbO 3-based lead-free dielectrics, *Sci. China Technol. Sci.*, 2026, **69**, 1320205.

8 M. Zhang, S. Lan, B. B. Yang, H. Pan, Y. Q. Liu, Q. H. Zhang, J. L. Qi, D. Chen, H. Su, D. Yi, Y. Y. Yang, R. Wei, H. D. Cai, H. J. Han, L. Gu, C.-W. Nan and Y.-H. Lin, Ultrahigh energy storage in high-entropy ceramic capacitors with polymorphic relaxor phase, *Science*, 2024, **384**, 185–189.

9 C. Li, J. Liu, L. Lin, W. Bai, S. Wu, P. Zheng, J. Zhang and J. Zhai, Superior Energy Storage Capability and Stability in Lead-Free Relaxors for Dielectric Capacitors Utilizing Nanoscale Polarization Heterogeneous Regions, *Small*, 2023, **19**, 2206662.

10 L. Chen, T. Hu, X. Shi, H. Yu, H. Zhang, J. Wu, Z. Fu, H. Qi and J. Chen, Near-Zero Energy Consumption Capacitors by Controlling Inhomogeneous Polarization Configuration, *Adv. Mater.*, 2024, **36**, 2313285.

11 W. Zhao, Z. Liu, D. Xu, G. Wang, D. Li, J. Liu, Z. Wang, Y. Guo, J. Ren, T. Zhou, L. Pang, H. Yang, W. Liu, H. Huang and D. Zhou, Advanced stability and energy storage capacity in hierarchically engineered $Bi_{0.5}Na_{0.5}TiO_3$-based multilayer capacitors, *Nat. Commun.*, 2025, **16**, 6549.

12 J. Hu, P. Wang, L. He, G. Ge, J. Liu, T. Hu, F. Xu, T. Zeng, Z. Fu, J. Zhai, W. Li and Z. Pan, Local heterogeneous dipolar structures drive gigantic capacitive energy storage in antiferroelectric ceramics, *Nat. Commun.*, 2025, **16**, 5535.

13 H. Zhao, W. Cao, C. Liang, C. Wang, C. Wang and Z. Cheng, High-Entropy Design Toward Ultrahigh Energy Storage Density Under Moderate Electric Field in Bulk Lead-Free Ceramics, *Adv. Funct. Mater.*, 2025, **35**, 2411954.

14 H. Liu, Z. Sun, J. Zhang, H. Luo, Y. Yao, X. Wang, H. Qi, S. Deng, J. Liu, L. C. Gallington, Y. Zhang, J. C. Neuefeind and J. Chen, Local Chemical Clustering Enabled Ultrahigh Capacitive Energy Storage in Pb-Free Relaxors, *J. Am. Chem. Soc.*, 2023, **145**, 19396–19404.

15 Z. Sun, H. Liu, J. Zhang, H. Luo, Y. Yao, Y. Zhang, L. Liu, J. C. Neuefeind and J. Chen, Strong Local Polarization Fluctuations Enabled High Electrostatic Energy Storage in Pb-Free Relaxors, *J. Am. Chem. Soc.*, 2024, **146**, 13467–13476.

16 B. Yang, Q. Zhang, H. Huang, H. Pan, W. Zhu, F. Meng, S. Lan, Y. Liu, B. Wei, Y. Liu, L. Yang, L. Gu, L.-Q. Chen, C.-W. Nan and Y.-H. Lin, Engineering relaxors by entropy for high energy storage performance, *Nat. Energy*, 2023, **8**, 956–964.

17 B. Xie, Q. Wu, C. Yu, S. Wu, J. Zhang, Z. Liu, K. Guo, H. Liu and T. Li, Local structure strategies promoting lead-free dielectric energy-storage applications, *Small*, 2026, **22**, e12097.

18 Y. Liu, Y. Zhang, J. Wang, C. Yang, H. Wang, J. L. MacManus-Driscoll, H. Yang, P. A. van Aken, W. Li and C.-W. Nan, Ultrahigh capacitive energy storage through dendritic nanopolar design, *Science*, 2025, **388**, 211–216.

19 H. Zhao, R. Xu, M. J. Wang, G. Wang, H. C. Sun, X. Z. Wang, Q. S. Zhu, X. Y. Wei, Y. J. Feng and Z. Xu, Excellent Energy Storage Performance of ZnO doped $(Pb,La)(Zr,Sn,Ti)O_3$ Based Antiferroelectric Ceramics at an Ultra-Low Sintering Temperature of 940 °C, *Adv. Funct. Mater.*, 2024, **34**, 2316674.

20 L. Chen, N. Wang, Z. Zhang, H. Yu, J. Wu, S. Deng, H. Liu, H. Qi and J. Chen, Local Diverse Polarization Optimized Comprehensive Energy-Storage Performance in Lead-Free Superparaelectrics, *Adv. Mater.*, 2022, **34**, 2205787.

21 J. Guo, H. Yu, Y. Ren, H. Qi, X. Yang, Y. Deng, S.-T. Zhang and J. Chen, Multi-symmetry high-entropy relaxor ferroelectric with giant capacitive energy storage, *Nano Energy*, 2023, **112**, 108458.

22 C. Long, Z. Su, A. Xu, H. Huang, L. Liu, L. Gu, W. Ren, H. Wu and X. Ding, $Bi_{0.5}Na_{0.5}TiO_3$-based energy storage ceramics with excellent comprehensive performance by constructing dynamic nanoscale domains and high intrinsic breakdown strength, *Nano Energy*, 2024, **124**, 109493.

23 M. Liu, H. Liu, Z. Liu, Z. Hu, K. Dai, S. Yan, Z. Hu and G. Wang, Superior energy-storage performance in $BaTiO_3$-$AgNbO_3$ binary relaxor via the competitions of multiple polar orders, *Acta Mater.*, 2025, **289**, 120943.

24 Q. Yuan, F. Z. Yao, S. D. Cheng, L. Wang, Y. Wang, S. B. Mi, Q. Wang, X. Wang and H. Wang, Bioinspired Hierarchically Structured All-Inorganic Nanocomposites with Significantly Improved Capacitive Performance, *Adv. Funct. Mater.*, 2020, **30**, 2000191.

25 D. Li, Z. Zheng, B. Yang, L. Chen, D. Shi, J. Guo and C. W. Nan, Atomic-Scale High-Entropy Design for Superior Capacitive Energy Storage Performance in Lead-Free Ceramics, *Adv. Mater.*, 2025, **37**, 2409639.

26 X. Zeng, J. Lin, J. Shen, Y. Chen, W. Xu, L. Tang, S. Wang, M. Gao, C. Zhao, T. Lin, L. Luo, C. Chen, B. Sa, C. Lin, X. Wu and J. Zhai, Giant Capacitive Energy Storage in High-Entropy Lead-Free Ceramics with Temperature Self-Check, *Adv. Mater.*, 2024, **36**, 2409059.

27 W. Cao, R. Lin, X. Hou, L. Li, F. Li, D. Bo, B. Ge, D. Song, J. Zhang, Z. Cheng and C. Wang, Interfacial Polarization Restriction for Ultrahigh Energy-Storage Density in Lead-Free Ceramics, *Adv. Funct. Mater.*, 2023, **33**, 2301027.

28 D. Tai, B. Li, H. Xue, T. Zheng and J. Wu, $BiFeO_3$-$BaTiO_3$ ferroelectrics: Decrypting the mechanism of rare earth doping-induced electrical property discrepancy via scaling behavior and multi-level structure, *Acta Mater.*, 2024, **262**, 119411.

29 H. Pan, S. Lan, S. Xu, Q. Zhang, H. Yao, Y. Liu, F. Meng, E.-J. Guo, L. Gu, D. Yi, X. Renshaw Wang, H. Huang, J. L. MacManus-Driscoll, L.-Q. Chen, K.-J. Jin, C.-W. Nan and Y.-H. Lin, Ultrahigh energy storage in superparaelectric relaxor ferroelectrics, *Science*, 2021, **374**, 100–104.

30 O. Paull, C. Xu, X. Cheng, Y. Zhang, B. Xu, K. P. Kelley, A. de Marco, R. K. Vasudevan, L. Bellaiche, V. Nagarajan and D. Sando, Anisotropic epitaxial stabilization of a low-symmetry ferroelectric with enhanced electromechanical response, *Nat. Mater.*, 2021, **21**, 74–80.

31 Z. Yang, Y. Li, J. Pan, B. Xie, K. Li, K. L. Moore, A. K. Kleppe and D. A. Hall, Effects of trace Nb dopant on core-shell microstructure and ferroelectric domain switching in $BiFeO_3$-$BaTiO_3$ ceramics, *Acta Mater.*, 2025, **289**, 120890.

32 H. Qi, G. Wang, Y. Zhang, D. Wang, H. Liu, S. Deng, R. Zuo and J. Chen, Tunable phase structure in $NaNbO_3$ ceramics by grain-size effect, electric field and heat treatment, *Acta Mater.*, 2023, **248**, 118778.

33 L. Chen, C. Zhou, L. Zhu, H. Qi and J. Chen, Compromise Optimized Superior Energy Storage Performance in Lead-Free Antiferroelectrics by Antiferroelectricity Modulation and Nanodomain Engineering, *Small*, 2023, **20**, 2306486.

34 J. Jiang, X. Li, L. Li, S. Guo, J. Zhang, J. Wang, H. Zhu, Y. Wang and S.-T. Zhang, Novel lead-free $NaNbO_3$-based relaxor antiferroelectric ceramics with ultrahigh energy storage density and high efficiency, *J. Materiomics*, 2022, **8**, 295–301.

35 Q. Chai, P. Tan, L. Zhang, Z. Liu, S. Dang, Z. Peng, D. Wu, X. Xu, B. Xing, X. Chao, H. Huang, S. Zhang and Z. Yang, Ultrahigh Energy Storage in Relaxor Ferroelectric Ceramics with Core–Shell Grains, *Adv. Funct. Mater.*, 2025, **35**, 2503798.

36 X. Dong, Z. Fu, Z. Wang, X. Lv and J. Wu, Engineering relaxors by embedding ultra-weak polar regions for superior energy storage, *Nat. Commun.*, 2025, **16**, 5657.

37 X. Xiong, H. Liu, J. Zhang, L. L. da Silva, Z. Sheng, Y. Yao, G. Wang, M. Hinterstein, S. Zhang and J. Chen, Ultrahigh Energy-Storage in Dual-Phase Relaxor Ferroelectric Ceramics, *Adv. Mater.*, 2024, **36**, 2410088.

38 D. You, H. Tan, Z. Yan, H. Gao, S. Chen, W. Ma, P. Fan, N.-M.-A. Tran, Y. Liu, D. Salamon and H. Zhang, Enhanced Dielectric Energy Storage Performance of $0.45Na_{0.5}Bi_{0.5}TiO_3$-$0.55Sr_{0.7}Bi_{0.2}TiO_3$/AlN 0–3 Type Lead-Free Composite Ceramics, *ACS Appl. Mater. Interfaces*, 2022, **14**, 17652–17661.

39 C. Zhao, S. Gao, T. Yang, M. Scherer, J. Schultheiß, D. Meier, X. Tan, H. J. Kleebe, L. Q. Chen, J. Koruza and J. Rödel, Precipitation Hardening in Ferroelectric Ceramics, *Adv. Mater.*, 2021, **33**, e2102421.

40 C. Zhu, A. Li, X. Li, S. Li, Z. Feng, Z. Cai, P. Feng and X. Wang, Ultra-stable dielectric properties and enhanced energy storage density of BNT-NN-based ceramics via precise core-shell structure controlling, *J. Alloys Compd.*, 2025, **1010**, 177556.

41 Y. Huan, X. Wang, Y. Zheng, X. Wang, T. Wei, J. Ouyang and X. Wang, Achieving excellent energy storage reliability and endurance via mechanical performance optimization strategy in engineered ceramics with core-shell grain structure, *J. Materiomics*, 2022, **8**, 601–610.

42 Y. Zhang, C. Yu, X. Zhou, Y. Jiang, G. Xue, Y. Zhang and D. Zhang, Phase structure and grain boundary engineering of BNT-based relaxor ferroelectric ceramics for high performance dielectric capacitors, *J. Energy Storage*, 2025, **115**, 115961.

43 B. Yang, Y. Liu, W. Li, S. Lan, L. Dou, X. Zhu, Q. Li, C. W. Nan and Y. H. Lin, Balancing Polarization and Breakdown for High Capacitive Energy Storage by Microstructure Design, *Adv. Mater.*, 2024, **36**, 2403400.

44 M. Ahart, M. Somayazulu, R. E. Cohen, P. Ganesh, P. Dera, H.-k. Mao, R. J. Hemley, Y. Ren, P. Liermann and Z. Wu, Origin of morphotropic phase boundaries in ferroelectrics, *Nature*, 2008, **451**, 545–548.

45 R. A. Cowley, Structural phase transitions I. Landau theory, *Adv. Phys.*, 2006, **29**, 1–110.

46 M. Waqar, H. Wu, J. Chen, K. Yao and J. Wang, Evolution from Lead-Based to Lead-Free Piezoelectrics: Engineering of Lattices, Domains, Boundaries, and Defects Leading to Giant Response, *Adv. Mater.*, 2021, **34**, 2106845.

47 G. Yu, X. Dong, G. Wang, F. Cao, X. Chen and H. Nie, Three-stage evolution of dynamic hysteresis scaling behavior in $63PbTiO_3-37BiScO_3$ bulk ceramics, *J. Appl. Phys.*, 2010, **107**, 106102.

48 R. Yimnirun, R. Wongmaneerung, S. Wongsaenmai, A. Ngamjarurojana, S. Ananta and Y. Laosiritaworn, Dynamic hysteresis and scaling behavior of hard lead zirconate titanate bulk ceramics, *Appl. Phys. Lett.*, 2007, **90**, 112908.

49 W. Cao, Y. Wu, X. Yang, D. Guan, X. Huang, F. Li, Y. Guo, C. Wang, B. Ge, X. Hou and Z. Cheng, Breaking polarization-breakdown strength paradox for ultrahigh energy storage density in NBT-based ceramics, *Nat. Commun.*, 2025, **16**, 6228.

50 Z. Zhou, W. Bai, N. Liu, W. Zhang, S. Chen, P. Wang, J. Liu, J. Zhai, J. Guo, G. Du, Y. Wu, Z. Hong, W. Li and Z. Pan, Ultrahigh capacitive energy storage of $BiFeO_3$-based ceramics through multi-oriented nanodomain construction, *Nat. Commun.*, 2025, **16**, 2075.

51 X. Zeng, J. Lin, G. Dong, J. Shen, L. Tang, Q. Lin, S. Wang, M. Gao, C. Zhao, T. Lin, L. Luo, C. Chen, B. Sa, C. Lin, X. Wu and J. Zhai, Polymorphic relaxor phase and defect dipole polarization co-reinforced capacitor energy storage in temperature-monitorable high-entropy ferroelectrics, *Nat. Commun.*, 2025, **16**, 1870.

52 Y. Yao, Z. Zhu, J. Zhang, H. Luo, L. Liu, J. Liu, J. C. Neuefeind, H. Liu and J. Chen, Adaptive Local and Global Structure Enabling Superior Capacitive Energy-Storage in Pb-Free Relaxors Under Moderate Electric Field, *Adv. Funct. Mater.*, 2025, **36**, e17831, DOI: 10.1002/adfm.202517831.

53 C. Long, Z. Su, A. Xu, H. Huang, L. Liu, L. Gu, W. Ren, H. Wu and X. Ding, $Bi_{0.5}Na_{0.5}TiO_3$-based energy storage ceramics with excellent comprehensive performance by constructing dynamic nanoscale domains and high intrinsic breakdown strength, *Nano Energy*, 2024, **124**, 109493.

54 Z. Sun, J. Zhang, H. Luo, Y. Yao, N. Wang, L. Chen, T. Li, C. Hu, H. Qi, S. Deng, L. C. Gallington, Y. Zhang, J. C. Neuefeind, H. Liu and J. Chen, Superior Capacitive Energy-Storage Performance in Pb-Free Relaxors with a Simple Chemical Composition, *J. Am. Chem. Soc.*, 2023, **145**, 6194–6202.

55 Y. Chen, Z. Zhu, L. Zhu, J. Xu, H. Luo, H. Li, W. Yin, L. Liu, J. Zhang, H. Liu and J. Chen, Giant Capacitive Energy-Storage in $BaTiO_3$-Based Fine-Grained Relaxors via Local Polarization Enhancement, *Adv. Mater.*, 2025, **37**, 2420566.

56 T. Deng, T. Hu, Z. Liu, C. Yao, K. Dai, F. Cao, Z. Hu and G. Wang, Ultrahigh energy storage performance in BNT-based binary ceramic via relaxor design and grain engineering, *Energy Storage Mater.*, 2024, **71**, 103659.

57 Q. Zheng, B. Xie, Y. Tian, Q. Wang, H. Luo, Z. Liu and H. Zhang, High recoverable energy density of $Na_{0.5}Bi_{0.5}TiO_3$-based ceramics by multi-scale insulation regulation and relaxor optimization strategy, *J. Materiomics*, 2024, **10**, 845–856.

58 H. Zhao, W. Cao, D. Han, X. Zhu, C. Liang, C. Wang and C. Wang, Suppressing interfacial polarization via entropy increase strategy for superior energy-storage performance of $Na_{0.5}Bi_{0.5}TiO_3$-based ceramics, *J. Materiomics*, 2024, **10**, 947–955.

59 B. Zhu, J. Zhang, F. Long, J. Liu, A. Sanson, L. Olivi, J. C. Neuefeind, H. Liu and J. Chen, Boosting Energy-Storage in High-Entropy Pb-Free Relaxors Engineered by Local Lattice Distortion, *J. Am. Chem. Soc.*, 2024, **146**, 29694–29702.

60 C. Kim, G. Pilania and R. Ramprasad, Machine Learning Assisted Predictions of Intrinsic Dielectric Breakdown Strength of ABX_3 Perovskites, *J. Phys. Chem. C*, 2016, **120**, 14575–14580.

61 J. Huang, S. Wang, Z. Zhang, M. Chen, H. Wang, H. Huang, Q. Wang, J. Hao, W. Li, J. Du, M. K. Joshi and P. Fu, Multiscale Structural Regulation of Energy Storage Properties and Their Mechanism of the $(1 - x)$ $(Bi_{0.5}Na_{0.5})_{0.7}Sr_{0.3}TiO_3 - xCa(Mg_{1/3}Ta_{2/3})O_3$ Ceramics, *ACS Appl. Mater. Interfaces*, 2025, **17**, 19938–19951.

62 L. Liu, Y. Liu, J. Hao, J. Chen, P. Li, S. Chen, P. Fu, W. Li and J. Zhai, Multi-scale collaborative optimization of $SrTiO_3$-based energy storage ceramics with high performance and excellent stability, *Nano Energy*, 2023, **109**, 108275.

63 W. Cao, T. Li, K. Li, Y. Huang, H. Xie, Y. Yao, Z. Sun, C. Lou, W. Zhang, C. Xu, L. Zhu, B. Xie, J. Zhang, M. G. Tucker, H. Liu, H. Luo, M. Tang and J. Chen, Unleashed Remarkable Energy Storage Performance in $Bi_{0.5}K_{0.5}TiO_3$-based Relaxor Ferroelectrics by Local Structural Fluctuation, *Angew. Chem., Int. Ed.*, 2024, **137**.

64 P. Li, H. Yang, Q. Yuan and Y. Lin, Enhanced energy storage performance of $Na_{0.5}Bi_{0.5}TiO_3$-based relaxor ferroelectric ceramics by synergistic optimization strategies, *Mater. Today Phys.*, 2024, **43**, 101420.